A new achievement in green degradation of aqueous organic pollutants under visible-light irradiation

Yadollah Abdollahi, Samad Sabbaghi, Ebrahim Abouzari-lotf, Hossein Jahangirian and Nor Asrina Sairi

ABSTRACT

The global attention has been focused on degradation of the environmental organic pollutants through green methods such as advanced oxidation processes (AOPs) under sunlight. However, AOPs have not yet been efficient in function of the photocatalyst that has been used. In this work, firstly, $CaCu_3Ti_4O_{12}$ nanocomposite was simultaneously synthesized and decorated in different amounts of graphene oxide to enhance photodegradation of the organics. The result of the photocatalyst characterization showed that the sample with 8% graphene presented optimum photo-electrical properties such as low band gap energy and a great surface area. Secondly, the photocatalyst was applied for photodegradation of an organic model in a batch photoreactor. Thirdly, to scale up the process and optimize the efficiency, the photodegradation was modeled by multivariate semi-empirical methods. As the optimized condition showed, 45 mg/L of the methyl-orange has been removed at pH 5.8 by 0.96 g/L of the photocatalyst during 288 min of the light irradiation. Moreover, the photodegradation has been scaled up for industrial applications by determining the importance of the input effective variables according to the following organics order > photocatalyst > pH > irradiation time.

Key words | graphene oxide, organic pollutants, photocatalyst, photodegradation, scale up, semi-empirical modelling

Yadollah Abdollahi (corresponding author)
Samad Sabbaghi
Nano Chemical Eng. Department,
Shiraz University,
Shiraz,
Iran
E-mail: *yabdollahi@gmail.com*

Ebrahim Abouzari-lotf
Advanced Materials Research Group,
Center of Hydrogen Energy,
Universiti Teknologi Malaysia,
Kuala Lumpur 54100,
Malaysia

Hossein Jahangirian
Department of Chemical Engineering, 313 Snell Engineering Center,
Northeastern University,
360 Huntington Avenue, Boston, MA 02115,
USA

Yadollah Abdollahi
Nor Asrina Sairi
Chemistry Department, Faculty of Science,
University of Malaya,
Kuala Lumpur 50603,
Malaysia

INTRODUCTION

The global attention has been focused on the removal of environmental aqueous organic pollutants using several methods, including biological oxidation systems, chemical and adsorption technology. However, the mentioned methods are limited by a few drawbacks; for instance, the biological methods are affected in longer retention time, the adsorption method is unable to mineralize the adsorbed pollutants from the environment and the chemical methods generate new toxic intermediates (Takeda & Teranishi 1988; Martino *et al.* 1995; Martino & Savage 1997; Aviam *et al.* 2004). On the other hand, advanced oxidation processes (AOPs) are able to mineralize the organics to harmless final products such as H_2O and CO_2 using a stable and non-toxic photocatalyst, suitable reaction time, appropriate light irradiation at ordinary temperature and atmospheric pressure. The photocatalysts included TiO_2, ZrO_2, SnO_2 and ZnO, which have been well-known for ultraviolet (UV) irradiation due to their wide band gap energy (Kansal *et al.* 2008). On the other side, sunlight is preferred in large-scale operations as it is more economical and safer than UV irradiation (Thuillier *et al.* 2003). Moreover, sunlight energy is available at more than 1.36 kW per square meter on the Earth's surface, consisting of the visible spectrum (47%), UV (7%) and other spectra (46%) (Fröhlich 2002). The visible spectrum wavelength is between 400 nm and 700 nm, and represents insignificant energy (1.77 to 2.76 eV) for electron excitation through the large band gap of the photocatalyst (3.2 to 3.5 eV). Therefore, several methods have been devised to harness excitation from the lower band gap, including doping coloured transition metal ions into the wide band gap structure of the photocatalyst to improve photocatalytic activity, coupling different semiconductors to enhance recombination time and synthesise the new short band gap and high surface area

doi: 10.2166/wst.2018.017

photocatalyst (Abdollahi *et al.* 2011b). As a result, the doped photocatalysts were more efficient than their original form under visible light. However, the photocatalyst yield performance is insufficient still, due to the relatively short time recombination of charge carriers. In other methods, coupling two photocatalysts with different band gaps has been used to enhance the separation time, which provides a significant opportunity to trap photo-generated charge carriers (Devi & Kavitha 2013). In this case, several works have been reported as follows: TiO_2 was successfully coupled with SiO_2, MoO_3, CdS, MgO, WO_3, SnO_2, Cu_2O, In_2O_3 and ZnO (Wu *et al.* 2006). Although the coupling method has promoted the efficiency of the photocatalyst, it is still insufficient for visible-light irradiation. On the other hand, the theoretical and experimental study of new photocatalysts such as $CaCu_3Ti_4O_{12}$ (CCTO) perovskite has been carried out to achieve materials that possess high activity in the visible range (Chen & Zhang 2010; Clark *et al.* 2010). Thus, CCTO is an ABO_3 materials with cubic double-perovskite structure with Ca^{2+} and Cu^{2+} on the A site and Ti^{4+} on the B site (Subramanian & Sleight 2002). The complex oxide of CCTO facilitates visible-light photocatalytic activity without requiring doping, which arises from charge transfer of Cu^{2+} and Ti^{4+} valence band (VB) to Cu^{3+} and Ti^{3+} conduction band (CB). The synthesized CCTO, which process a suitable band gap energy (1.93 and 2.21 eV), was used as photocatalyst to aid degradation of organic water pollutant by AOPs, under visible-light irradiation ($700\ nm < \lambda > 400\ nm$) (Clark *et al.* 2010). However, the average surface area of the photocatalyst was quite low ($8.33\ m^3/g$), while the average particle size was in the nano-scale region, 70.15 nm. Consequently, the photodegradation efficiency was insufficient under visible-light irradiation. On the other hand, reduced graphene oxide (RGO) has presented excellent specific surface area, which enhances the surface of the photocatalyst (Sun *et al.* 2014).

MATERIALS AND METHODS

In this work, CCTO was simultaneously synthesized and decorated in different percentages of RGO to prepare CCTO-RGO nano-composites. Thereafter, the final photocatalyst with optimized properties was selected to apply for degradation of methyl orange (MO) as a model of organic environmental pollutants under artificial day time sunlight. To optimize and scale up the degradation, the application was modeled by multivariable methods such as response surface methodology (RSM) and then artificial neural networks. Such multivariate methods are preferred to the single variable approach due to the increase in the dimensionality of the system and production of more generalized results (Abdollahi *et al.* 2013a).

Synthesis of photocatalyst

The CCTO was simultaneously synthesized and decorated in graphene oxide (GO) by the chemical sol-gel method. In this method, equal amounts of Titanium(IV) bis (ammonium lactato) dihydroxide solution (50 wt. % in H_2O), calcium acetate (99%) and copper acetate (99%) were dissolved in five containers of deionized (DI) water as five blank solutions and magnetically stirred for 45 min. Then the appropriate volume of GO (4 mg/mL, water dispersion 1,000 mL) was slowly added to the solutions over half an hour. The effect of GO was included at 0, 4, 6, 8 and 10 weight (wt%) for five samples that were called CCTO-GO (0%), CCTO-GO (4%), CCTO-GO (6%), CCTO-GO (8%), and CCTO-GO (10%). Thereafter, the appropriate amount of porcine skin gelatine powder was dissolved in the samples. The solutions were stirred for 30 min at 70 °C and then evaporated at 90 °C with continuous stirring. The produced paste-like mixture was dried in a hot oven for 8 hours at 150 °C. The dried paste was ground and sieved and the fine powder was calcined at two steps, 350 °C then at 400 °C for 3 hours in the air to burn the gelatine, and generate nanoparticles of CCTO and RGO. The heating and cooling rate were performed at 5 °C/min according to recording of Thermal Gravimetric Analysis (TGA) in a box furnace (cable modem termination system (CMTS) model high-temperature stage (HTS) 1400). The calcination was confirmed by Fourier-transform infrared spectroscopy (FTIR) spectra, which were obtained by Fourier Transform Infrared Spectrometer Nicolet 6,700 (Thermo Nicolet Corp., Madison, WI) equipped with a deuterated triglycine sulfate detector. The samples were characterized by X-ray diffraction (XRD) (PANanalytica, Philips-X'pert Pro PW3040/60). Their electrical properties were determined by UV-visible absorption and diffuse reflectance (Ref %). The Ref % data of the powder samples was provided by Perkin Elmer Lambda 35 UV-Vis-NIR equipped with a Labsphere integrating sphere over the spectral range of 200 to 900 nm. The spectra were analyzed by using the Kubellka-Munk function (Ye & Ohmori 2002). The transmittance electron microscopy (TEM) images were obtained by using a Hitachi H-7100 electron microscope. The field emission scanning electron microscopy (FESEM) morphology and energy dispersive X-ray analysis (EDX) analysis were obtained from JEOL JSM-6400 instruments.

Photodegradation set up

Regarding the characterization, a CCTO-RGO (8%) sample has been selected as the photocatalyst, and methyl orange (System brand) was used as model of the environmental aqueous organic pollutant. The performance has been started according to the experimental design (Table 1) by mixing various concentrations of MO with appropriate amount of the photocatalyst in 300 ml DI water. The mixture solutions (suspension) were irradiated by a Philips lamp (23 W) as the light source in a designed batch photoreactor that was used in our previous work (Abdollahi *et al.* 2012a). The suspensions were magnetically stirred during the irradiation at 200 rpm. To increase solution fluidization, access oxygen, volatilize the produced gas and kept the temperature at around 25 °C, air was blown into the solution by using an air pump. During the operation, samples were withdrawn from the bulk solution at specific time intervals, centrifuged at 4,000 rpm for 30 min and then filtered through 0.2 μm polytetrafluoroethylene (PTFE) membrane to measure the remaining concentration of the MO.

For each sampling, the evaporated volume of the suspension solution was measured by a crystal-pump that was not involved with the solution. The evaporated volume of the solution was properly replaced. The remained concentration of the MO was measured by a spectrophotometer (Shimadzu UV-1650 PC) at a wavelength of 465 nm. The efficiency was calculated by Equation (1).

$$\text{Efficiency } (\%) = (C_0 - C_t) \times \frac{100}{C_0} \quad (1)$$

where C_0 is initial concentration and C_t is the final concentration of MO in each operation. The efficiencies were used as actual responses for semi-empirical modeling of the photodegradation, which was carried out by RSM and ANN. The performance was carried out according to an experimental design based on our previous publications (Abdollahi *et al.* 2013b).

Table 1 | The experimental design of the photodegradation of methyl orange by CCTO-GO (8%), the actual efficiency is the observed result while the predicted efficiency was provided by a fitting process in RSM; the number of experiments was 29, which consists of the factorial points (16), the axial points (7) and the replications (6), the run presents the number of the experiment

Run	Time (min)	pH	CCTO (mg/L)	MO (g/L)	Actual efficiency (%)	Predicted efficiency (%)
1	180	4.5	0.5	25	47	58
2	300	4.5	0.5	25	65	48
3	180	6.5	0.5	25	70	46
4	300	6.5	0.5	25	85	99
5	180	4.5	1.5	25	65	99
6	300	4.5	1.5	25	90	63
7	180	6.5	1.5	25	75	55
8	300	6.5	1.5	25	100	100
9	180	4.5	0.5	45	35	99
10	300	4.5	0.5	45	56	84
11	180	6.5	0.5	45	59	66
12	300	6.5	0.5	45	78	99
13	180	4.5	1.5	45	35	56
14	300	4.5	1.5	45	63	99
15	180	6.5	1.5	45	43	78
16	300	6.5	1.5	45	73	72
17	120	5.5	1	35	47	34
18	360	5.5	1	35	91	36
19	240	3.5	1	35	25	91
20	240	7.5	1	35	55	54
21	240	5.5	2	35	84	99
22	240	5.5	1	15	94	91
23	240	5.5	1	55	53	64
24	240	5.5	1	35	99	70
25	240	5.5	1	35	98	86
26	240	5.5	1	35	99	44
27	240	5.5	1	35	100	24
28	240	5.5	1	35	99	75
29	240	5.5	1	35	100	93

RESULTS AND DISCUSSION

Characterization

Optical properties

Figure 1 shows the UV-visible absorption of the CCTO-RGO samples, including CCTO-RGO (0%), CCTO-RGO (4%), CCTO-RGO (6%), CCTO-RGO (8%) and CCTO-RGO (10%). As observed, all of the samples presented absorption in the visible area of wavelength (400 to 600 nm); however, the CCTO-RGO (8%) has illustrated a sharp slope of absorption in the region (curve (b) in Figure 1). In addition, Table 2 shows the calculated band gap of the samples. The band gaps were calculated by the Kubelka-Munk function, which used diffuse reflectance spectra of the powder (Ye & Ohmori 2002). As indicated, samples CCTO-RGO (0%) and

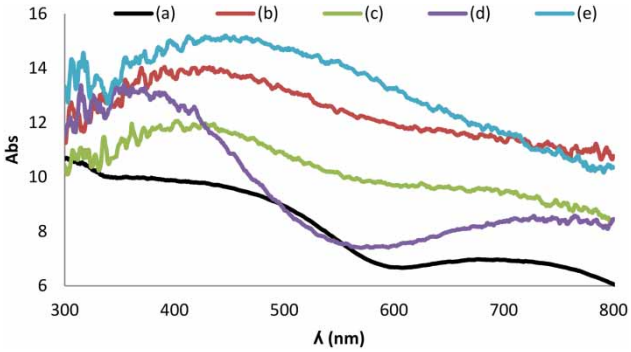

Figure 1 | The UV-visible absorption of the synthesized photocatalysts, (a) CCTO-RGO (0%), (b) CCTO-RGO (8%), (c) CCTO-RGO (6%), (d) CCTO-RGO (4%) and (e) CCTO-RGO (10%).

Table 2 | The band gap energy and BET surface area of the synthesized samples, B.G is band gap

Sample	CCTO-RGO (0%)	CCTO-RGO (4%)	CCTO-RGO (6%)	CCTO-RGO (8%)	CCTO-RGO (10%)
B.G (eV)	2.1 & 2.7	1.5	1.7	1.5 & 2.1	1.7
BET (m^2/g)	10.1	38.5	47.2	130.4	57.0

CCTO-RGO (8%) have presented two distinct band gaps that are well comparable with reported values (Rakhshani & Barakat 1987). As reported, mostly $CaCu_2Ti_4O_{12}$ has two band gaps due to transition metals compounds such as Cu and Ti (Clark *et al.* 2010). The reported band gap was 2.0 eV, which is in the middle of the visible-light energy ($\lambda = 400$ to 500 nm). In addition to the electrical properties, as Table 2 shows, the Brunauer–Emmett–Teller (BET) surface area of CCTO-RGO (8%) samples was at maximum value in comparison with the other sample's BETs surface area, which confirmed its effectiveness under visible-light irradiation. Therefore, the CCTO-RGO (8%) sample was selected for further characterization such as XRD, EDX, FTIR, TEM and FESEM.

Figure 2 shows the XRD patterns phase determination analysis of the CCTO-RGO (8%) sample. The phases were analysed according to the corresponding 2θ characteristic values of their diffraction peaks. Therefore, $CaCu_3Ti_4O_{12}$ was identified by reference 01-070-0609 (Propach 1977), while the small amounts of CuO and TiO_2 were also identified by 01-089-5895 and 00-065-1118 references respectively. As indicated, $CaCu_3Ti_4O_{12}$ is the main product, while a small amount of CuO and TiO_2 was identified as impurity contents.

Moreover, the FTIR spectra of CCTO-RGO (8%) before and after calcination have been compared and are in agreement with a previous report (Titelman *et al.* 2005). As observed, there is no peak for epoxy functional groups (C-O-C) on the calcinated sample. The epoxy groups peak of single layer graphene oxide is to be reported between 800 to 850 cm^{-1} and also 1,200 to 1,250 cm^{-1} (Acik *et al.* 2010). Therefore, it can be concluded that the GO was reduced to RGO during the calcination process.

Morphology

Figure 3 shows the FESEM morphology and EDX of the CCTO-RGO (8%) sample. As Figure 3(a) indicates, CCTO particles have been homogenized and dispersed inside the sheets

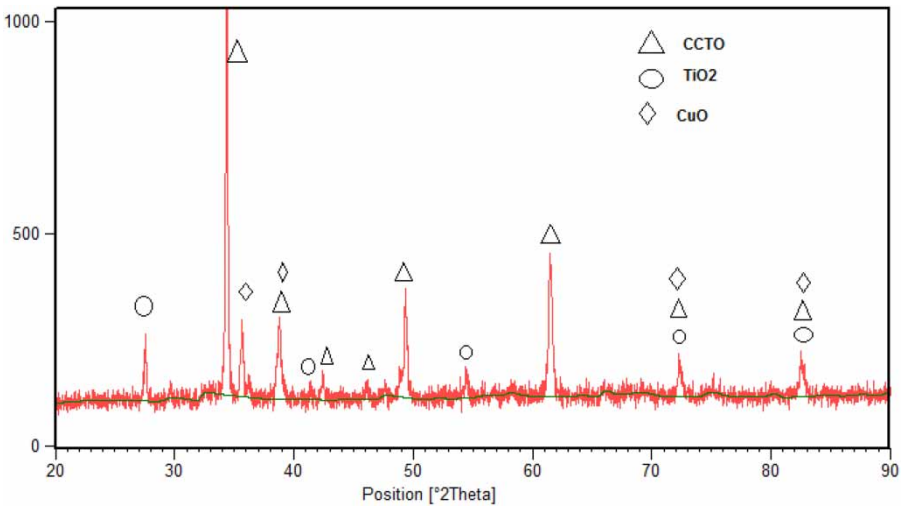

Figure 2 | The XRD patterns phase determination analysis of CCTO-RGO (8%) samples, Δ is $CaCu_3Ti_4O_{12}$, O is TiO_2 and ◊ is CuO.

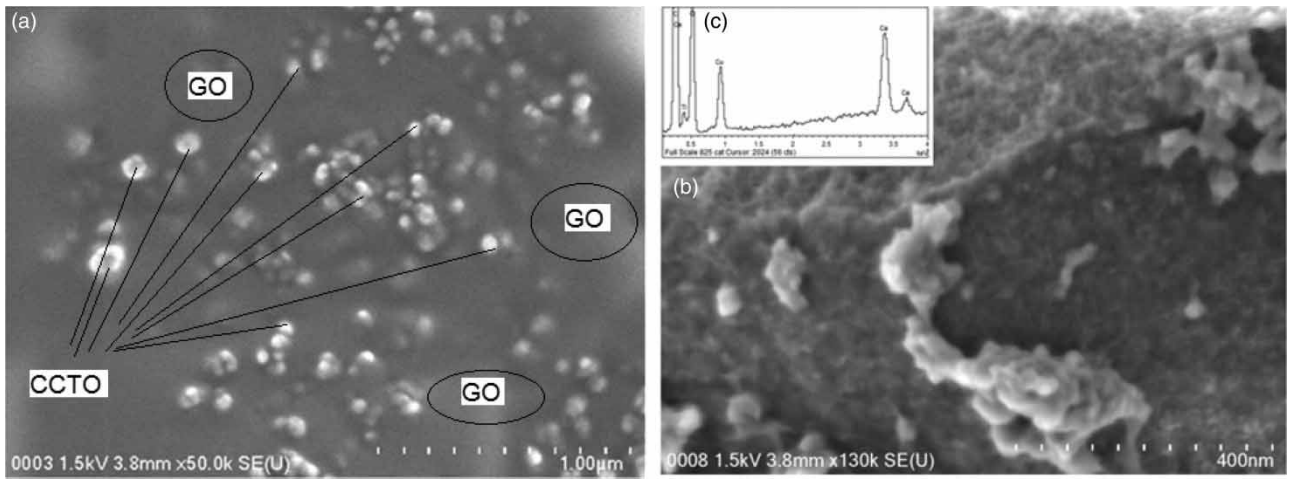

Figure 3 | FESEM morphology and EDX of the CCTO-RGO (8%) sample, (a) CCTO particles inside the GO sheets, (b) CCTO particles over the GO sheet, (c) EDX element analysis of the sample.

of RGO. Moreover, Figure 3(b) depicts a piece of agglomerated CCTO over GO sheet. Therefore, the CCTO particles were decorated both inside and outside (over) of the RGO sheets. In addition, EDX element analysis of the sample is presented in Figure 3(c), which confirmed the initial elements used, including Ca, Cu, Ti and O in a large area of CCTO-RGO (8%). Table 3 presents carbon of the GO sheets. As observed, the percentage of calcium is less than the stoichiometry of CCTO, which may be due to the presence of TiO_2 and CuO respectively on XRD investigation (Figure 2).

Table 3 | EDX element weight and atomic % of a large area of sample CCTO-RGO (8%)

Element	Calcium	Copper	Titanium	Oxygen	Carbon
Weight%	1.4	27.01	28.01	17.84	25.74
Atomic%	0.81	9.88	13.59	25.92	49.8

TEM

Figure 4 shows TEM images of the synthesized mesoporous CCTO-GO nano-composite matrix structure that presents an excellent uniform particle size. The TEM images are in very good agreement with the morphology that is presented in FESEM to confirm dispersion of CCTO particles in the sheets of GO (Figure 3). Figure 4(a) shows the sheets of GO that were decorated by CCTO particles, while

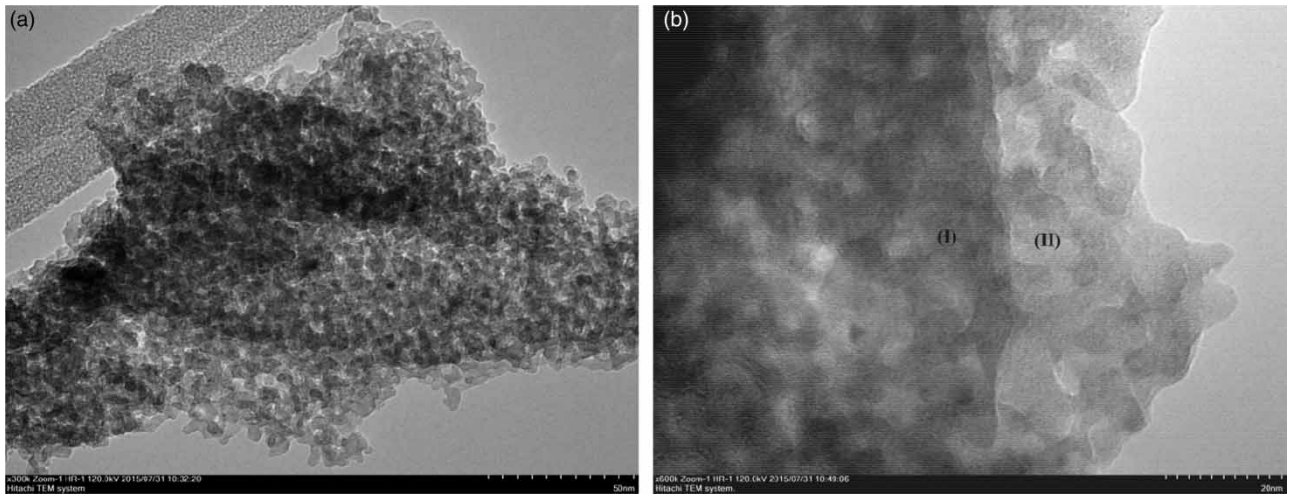

Figure 4 | TEM image of the synthesized CCTO-RGO nano-composite as photocatalyst, (a) the decorated of CCTO into the sheets of RGO, (b) TEM of both decorated CCTO into RGO (I) and CCTO without GO (II).

Figure 4(b) shows both decorated sheet (I) and CCTO particles without GO sheets (II). The average particle size of CCTO-RGO, which was calculated from the TEM images, was 5.3 nm.

Photodegradation

The mentioned characterization result of CCTO-RGO (8%) has confirmed its merit as a visible active photocatalyst; therefore, it was selected for degradation of MO as a model of organic pollutants under artificial visible-light irradiation. For this purpose, the preliminary experiments for the photodegradation, including the initial photocatalyst absorption and photolysis, were investigated in the dark and the absence of the photocatalyst at pH 6. The obtained results were considered in the final efficiencies calculation (Abdollahi *et al.* 2014b). The maximum interaction between the surface of the photocatalyst and MO was determined to be around pH 6 (Clark *et al.* 2010).

RSM analysis

RSM has been used to obtain the optimized level of the effective input variables. Initially, RSM used the actual efficiencies as output responses for the fitting process to suggest a suitable model for the photodegradation process. The methodology of the fitting process has been performed similarly to our previous work (Dorraj *et al.* 2015). As a result, the quadratic model was suggested by the software. Therefore, the authors have followed the software's suggestion and selected the quadratic model as the provisional model for more validation.

The provisional model has presented the relationship between the input variables themselves and the variables, efficiency using the estimated coefficients and linking (±) signs as a model (Equation (4)). In the presented model (Equation (4)), x_1 is irradiation time, x_2 is pH, x_3 is the amount of photocatalyst and x_4 is the amount of MO.

$$\begin{aligned} Y = {} & -647.02 + 1.03\,x_1 + 173.25\,x_2 + 97.20\,x_3 + 3.80\,x_4 \\ & - 0.003\,x_1\,x_2 + 0.07\,x_1\,x_3 + 0.002\,x_1\,x_4 - 6.31\,x_2\,x_3 \\ & + 0.0031\,x_2\,x_4 - 0.96\,x_3\,x_4 - 0.002\,x_1^2 - 14.42\,x_2^2 \\ & - 20.02\,x_3^2 - 0.06\,x_4^2 \end{aligned} \quad (2)$$

where Y is the efficiency; x_1, x_2, x_3 and x_4 are linear parameters, x_1^2, x_2^2, x_3^2 and x_4^2 are the quadratic terms, while x_1x_2, x_1x_3, x_1x_4, x_2x_3, x_2x_4, and x_3x_4 are the interaction factors (Dorraj *et al.* 2015). The estimated coefficients are the weights of the parameters, and the linked signs (+,−) determine the synergic and antagonistic behavior of the parameters in the model. The parameters in Equation (4) were validated by one-way analysis of variance (ANOVA), which showed the general model fit and lack of fit were correctly significant and not-significant respectively. As the details of the validation show, all the terms have presented a significant effect except the interaction of time and pH (x_1x_2) and pH and MO (x_2x_4), which were not effective factors and therefore they can be removed from the model. The importance of the parameters was determined according to our previous work (Dorraj *et al.* 2014), which showed pH was very important while the concentration of photocatalyst presented a secondary level of importance.

The validated model has optimized the input variables to show the maximum possible values of the efficiency in the range of the experimental design. The optimization was carried out by mathematical derivation of the validated model (Equation (4)). The derivation was obtained by Equations (5) to (8), in which only one parameter was varied (Abdollahi *et al.* 2012b).

$$\left[\frac{\partial Y}{\partial x_1}\right]_{x_1x_3x_4} = 0 \quad (3)$$

$$\left[\frac{\partial Y}{\partial x_2}\right]_{x_1x_3x_4} = 0 \quad (4)$$

$$\left[\frac{\partial Y}{\partial x_3}\right]_{x_1x_2x_4} = 0 \quad (5)$$

$$\left[\frac{\partial Y}{\partial x_4}\right]_{x_1x_2x_3} = 0 \quad (6)$$

These optimum points were used to determine the new levels of the variables in the experimental design by the model. The model was used to determine the level of the effective variables. The input variables' contour plots studies on the photodegradation efficiency (efficiency) have presented the effective level of pH as 5.3 to 6.3, while the optimum irradiation time was determined to be from 240 to 335 min. The best amount of photocatalyst was 0.7 to 2 g/L and the level of MO concentration was obtained as being from 20 to 40 mg/L. In the range of the experimental design, the simultaneous effects of two variables on the efficiency were considered as the 3D plot while the other parameters were kept constant at the points that were determined by Equations (5) to (8). Moreover, the model was used to determine the interaction of the effective variables. The 3D plots in Figure 5 show the simultaneous effect of pH with irradiation time (a),

pH with photocatalyst amount (b), pH with concentration of MO (c) and effect of photocatalyst amount and concentration of MO on the photodegradation efficiency (d). As 3D plots (a), (b) and (c) show, the maximum effect of the pH was determined to be around the point of 6 for all ranges of irradiation time, photocatalyst amount and concentration of MO. The efficiency was increased with increasing irradiation time and the optimum appeared above 240 min (Figure 5(a)). The optimum amount of photocatalyst was obtained as above 1 g/L due to the enhancement of photocatalyst active sites (Figure 5(b)), while the optimum value of MO concentration was 40 mg/L (Figure 5(c)) (Abdollahi *et al.* 2011a). Furthermore, the model was used for navigation of the photodegradation to obtain the maximum efficiency by using a numerical particular condition. The option was facilitated by the default of the software used. The particular condition was included as the 'in range option' for irradiation time, photocatalyst amount and pH, while the option of 'maximum' was selected for concentration of MO and the efficiency. Therefore, the predicted values for better efficiency of each variable were irradiation time (288 min), pH (5.8), photocatalyst amount (0.96 g/L) and MO concentration (45 mg/L), while the predicted efficiency was 89%. The condition was experimentally validated and the results were quite close to the prediction with 5.6% error.

ANN modeling

An ANN has been used to determine the importance of the degradation input effective variables. As observed, the Root Mean Squared Error (RMSE) from the learning process versus node number of the hidden layer of the ANN structures for quadratic programming (QP), batch back-propagation (BBP), incremental back-propagation (IBP) and Levenberg-Marquardt (LM) algorithms were compared (Abdollahi *et al.* 2014a). The node numbers are the number of the nodes in the hidden layer of the architectures. For each algorithm, there are 20 architectures where one of them has presented the lowest value of RMSE (topology). The topologies included were QP with 14 nodes (QP-4-14-1), BBP with 12 nodes (BBP-4-12-1), IBP with 13 nodes (IBP-4-13-1) and LM with 10 nodes

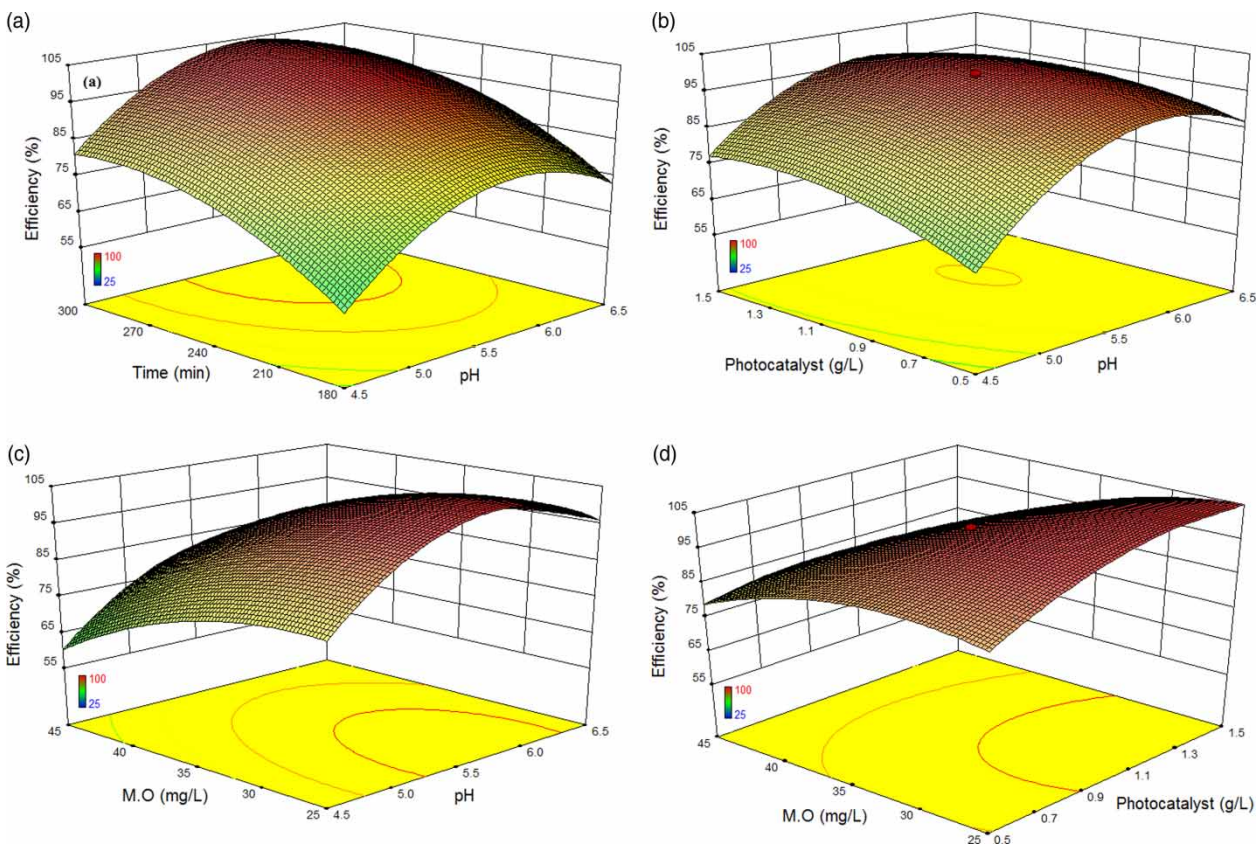

Figure 5 | The 3D plots of the effective variables interactions, (a) effect of pH and irradiation time, (b) interaction between pH and photocatalyst amount, (c) interaction between pH and concentration of MO, (d) interaction between photocatalyst amount and concentration of MO.

(LM-4-10-1). Among them, QP-4-14-1 topology illustrated the minimum RMSE (2.661); however, they were compared by calculated percentage of absolute average deviation (AAD) and R^2 to select the final model for the photodegradation (Table 4). Table 4 shows the results of AAD calculation for QP-4-14-1, BBP-4-13-1, IBP-4-12-1 and LM-4-10-1 and QP-4-14-1 topologies in training, testing and validation datasets. Among the topologies, QP-4-14-1 has presented the lowest AAD in the all three datasets that exhibited a reasonable AAD.

Table 4 | The calculated AAD for the topologies of QP-4-14-1, BBP-4-13-1, IBP-4-12-1 and LM-4-10-1in training, testing and validation datasets

Topology	Training	Testing	Validation
QP-4-14-1	0.007	4.544	0.479
BBP-4-13-1	0.465	7.539	1.126
IBP-4-12-1	0.178	9.178	1.767
LM-4-10-1	0.595	9.190	0.744

To compare the R^2 of the selected topologies, the actual efficiencies of the experiments were plotted versus the training predicted efficiencies of QP-4-14-1, BBP-4-13-1, IBP-4-12-1 and LM-4-10-1 topologies (Figure 6). As shown, all obtained values for the R^2s in the training dataset were acceptable; however, the predicted values of QP-4-14-1 topology were 100% fitted to the actual values ($R^2 = 1$).

According to the similar calculations for testing the dataset, QP-4-14-1 topology has presented the highest value of R^2, which confirmed the training dataset. Moreover, R^2 was also calculated for the topologies in the validation dataset. The results show that QP-4-14-1 topology depicted the highest value of the R^2 (0.975).

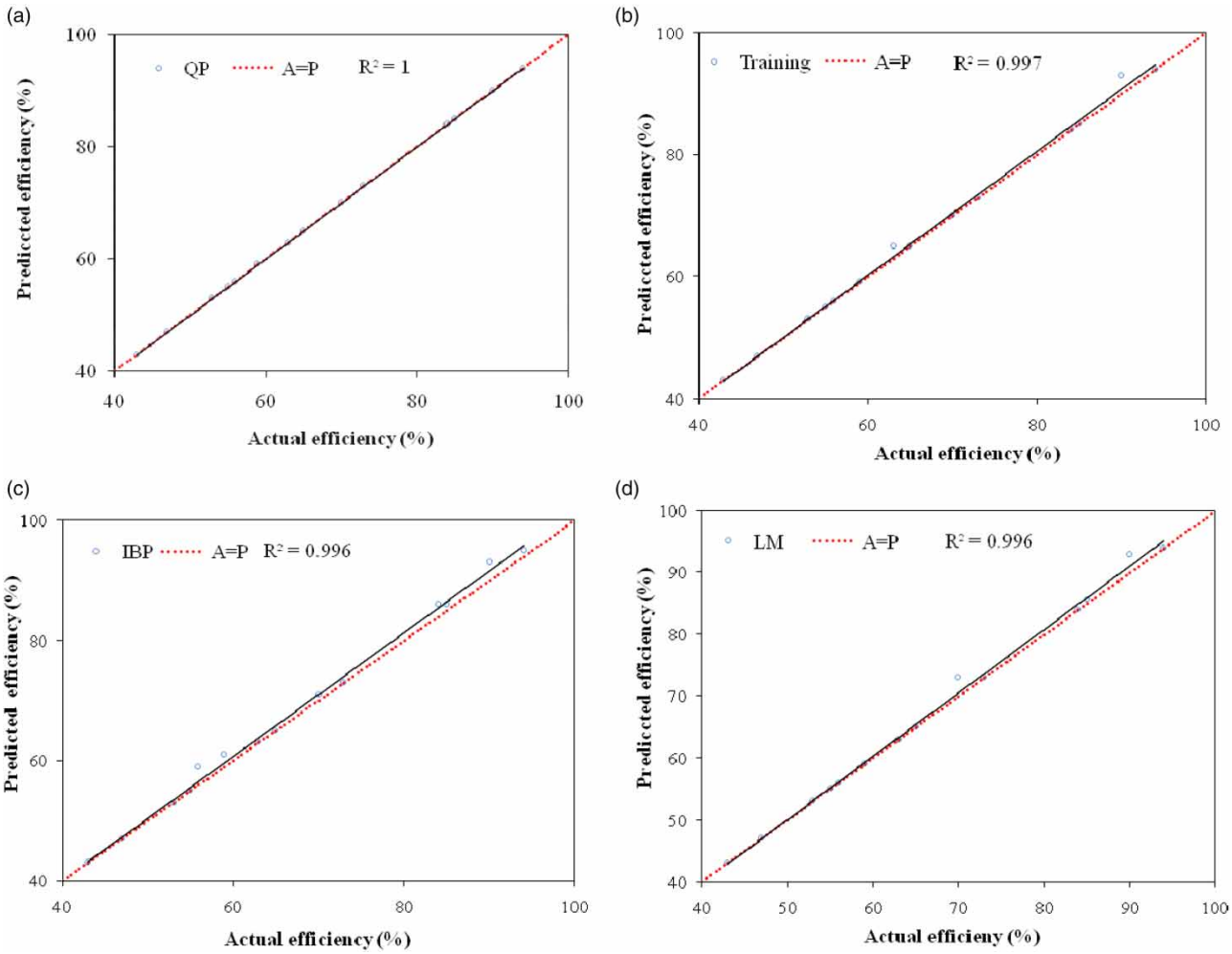

Figure 6 | The scatter plots of the predicted vs. actual efficiency of the learned training dataset to visualize the R^2 of selected topologies, (a) QP-4-14-1, (b) BBP-4-13-1, (c) IBP-4-12-1 and (d) LM-4-10-1, A = P is the best line.

Therefore, the QP-4-14-1 topology was selected as an efficient final model for the photodegradation due to having the lowest RMSE and AADs (Table 4) as well as the highest R^2s (Figure 6).

Figure 7 presents the structure of the selected topology as the final model (QP-4-14-1), which consists of four nodes in the input layer including irradiation time, pH, photocatalyst amount and MO concentration, while the efficiency of the photodegradation is only the node in its output layer. As observed, the determined nodes in the hidden layer content of 14 nodes, which connected to the nodes of the input and output layers by multilayer normal feed-forward, and the bias shifts the space of the efficiency (Ghaffari *et al.* 2006). As a result, the model was used to obtain the importance of the input variables. Moreover, the model predicted the optimum condition of photodegradation with maximum efficiency.

Figure 8 shows the 3D plots of the input variables' simultaneous effect on the efficiency as the only output of the photodegradation process.

In the 3D plots, the red color is the desirable area, the blue color shows the area with lowest values and yellow color is minimum applicable value of the efficiency which is based on determined optimized level of the variables. Figure 8(a) shows the simultaneous effect of photocatalyst amount (g/L) and time of irradiation (min) on the efficiency while the value of the pH (= 5) and concentration of MO (40 mg/L) were kept constant. As the bordering line (yellow color) shows, the level of the photocatalyst amount was 0.95 to 1.7 g/L while the level of irradiation time was 250 to 300 min. Figure 8(b) illustrates the effect of MO concentration (mg/L) and irradiation time on the efficiency, while the value of the pH and photocatalyst amount was kept constant at 5.00 and 1.25 g/L respectively. According to the bordering line, the level of the MO concentration was less than 40 mg/L and the level of the irradiation time was the same as mentioned in level in Figure 8(a). Figure 8(c) depicts the simultaneous effect of pH and irradiation time as variables while the concentration of MO (40 mg/L) and photocatalyst (1.25 g/L) were kept constant. As shown, the level of the pH was 5 to 5.8 and the level of the irradiation time in the previous plots was confirmed. Figure 8(d) shows the effect of the photocatalyst amount and pH on the photodegradation efficiency in the presence of the constant amount of MO (40 mg/L) and at 240 min of irradiation time. The determined level for photocatalyst and pH were 0.95 to 1.7 and 5.0 to 5.8 respectively. Figure 8(e) presents the effect of MO and photocatalyst on the efficiency in pH 5 and at 240 min of irradiation time. The observed level for MO and photocatalyst concentration confirmed the reported levels in the previous plots. Figure 8(f) exhibits the effect of MO and pH on the efficiency, which shows the level of the pH was larger than the reported values in Figure 8(c) and 8(d). The high value of the efficiency at the lower pH could be an advantage for low concentrations and pH of acidic wastewater.

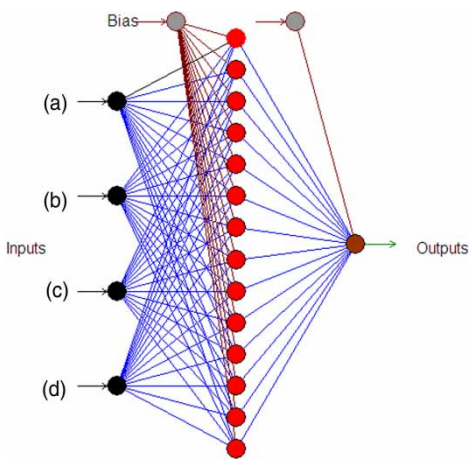

Figure 7 | The final model (QP-4-14-1) of the photodegradation of MO by CCTO-RGO under visible light irradiation, the inputs are included (a) irradiation time, (b) pH, (c) amount of photocatalyst and (d) concentration of MO while the output is the efficiency of the photodegradation.

The relative importance of the input effective variables of the photodegradation indicates the relative effect of them on the efficiency. As observed, all the variables are not ignorable and the order of importance of the variables has been included as MO > photocatalyst > pH > irradiation time. This order proved that the concentration of MO is the most important factor in the photodegradation. Moreover, the model (QP-4-14-1) predicted efficiency for five runs of the optimum condition at different irradiation times (Table 5). Then the runs were validated by further experiment. As shown, the obtained efficiencies were very close to the predicted efficiency. Particularly, the obtained result of the second run has confirmed the RSM's prediction as mentioned in the previous sections.

The result of multivariate modeling

Table 6 shows the compared level of the input variables, which were modeled by RSM and ANN processing. As observed, the order of calculated input variable levels is 'one variable at a time' > RSM > ANN. The narrowest level is more accurate than the wider level. The other achievement of the multivariate methods is the

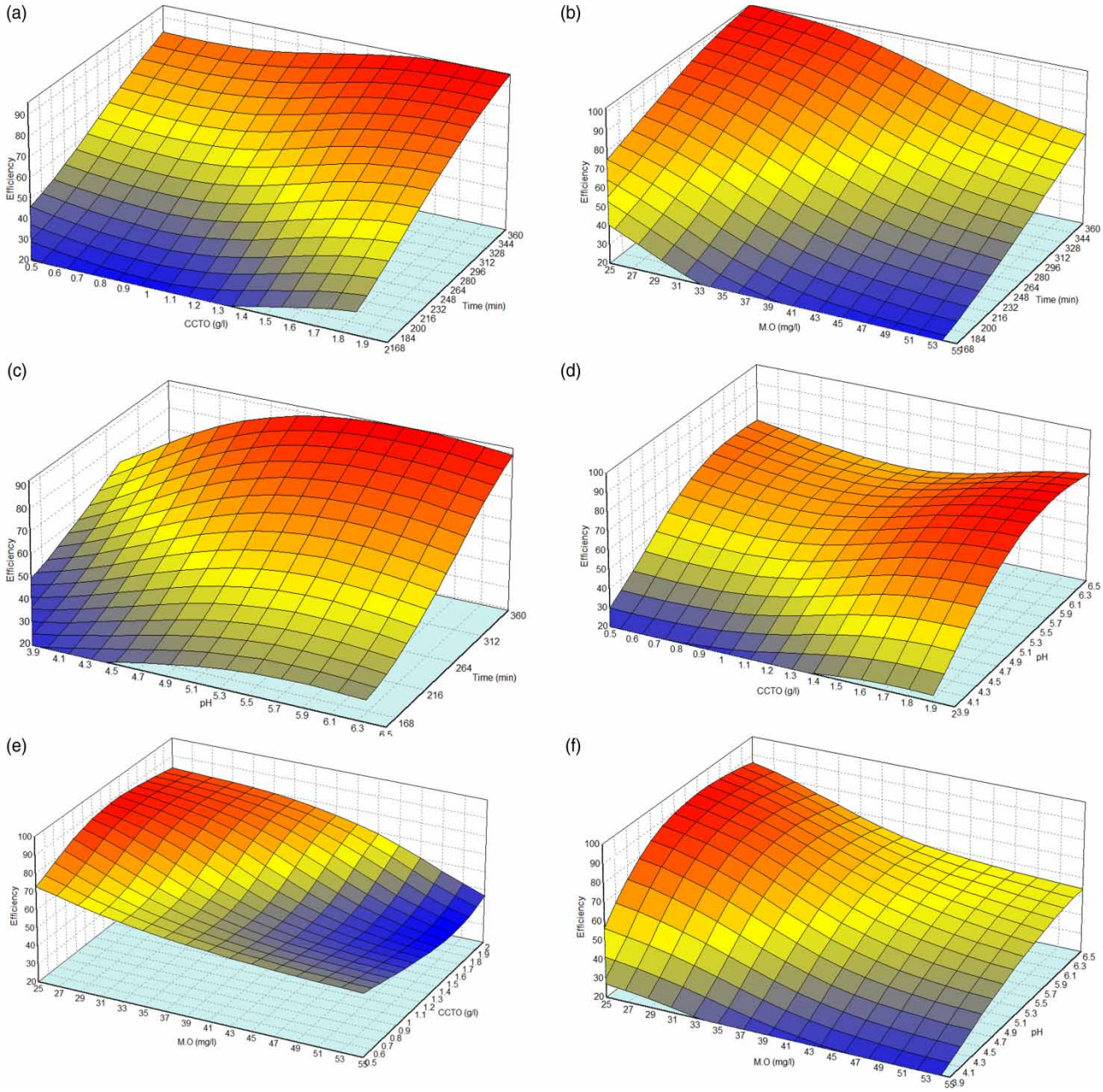

Figure 8 | The ANN 3D plots of multieffect of two inputs on the efficiency, (a) effect of photocatalyst and time, (b) effect of MO and time, (c) effect of pH and time, (d) effect of photocatalyst and pH, (e) effect of MO and photocatalyst, (f) effect of MO and pH on the efficiency; the red surface response is desirable, while the blue color shows the area with lowest values and yellow color is minimum applicable value of the efficiency. The full colour version of this figure is available in the online version of this paper, at http://dx.doi.org/10.2166/wst.2018.017.

determination of the effective input variables' optimum amount. Therefore, the optimum values of the RSM calculation are included as irradiation time (288 min), pH (5.8), photocatalyst amount (0.96 g/L) and MO concentration (45 mg/L), which were experimentally validated. As Table 6 shows, the optimum values have been confirmed by ANN model (QP-4-14-1), which indicates the methods confirm each other. Moreover, the importance of the input variables that can be useful for industrial scaling up were determined by ANN. The ANN importance order is MO >photocatalyst > pH> irradiation time, while the RSM has reported two kinds of importance order, including linear pH >photocatalyst > MO> irradiation time and for the quadratic as photocatalyst >pH > MO> irradiation time.

Table 5 | The model (QP-4-14-1) predicted efficiency for optimum condition of RSM modeling at different irradiation times

Run no.	1	2	3	4	5
Time (min)	264	288	312	336	360
pH	5.8	5.8	5.8	5.8	5.8
CCTO (g/L)	0.96	0.96	0.96	0.96	0.96
MO (mg/L)	45	45	45	45	45
Predicted efficiency (%)	75	83	85	89	92
Validated efficiency (%)	78	85	87	89	93

Table 6 | The level of input variables of photodegradation in initial experimental deign (E. D); obtained by RSM and ANN

	Level			
Source	Irradiation time (min)	pH	Photocatalyst (g/L)	MO (mg/L)
RSM	245–345	5.3–6.3	0.7–2.0	37 <
ANN	250–300	5–5.8	0.95–1.7	40 <

As observed, the factor of irradiation time is was not relatively important in either calculation, while other factors were very important as input effective variables.

CONCLUSION

To enhance visible-light photocatalytic activities, $CaCu_3Ti_4O_{12}$ nanocomposite with a high surface area was simultaneously synthesized and decorated in different percentages of GO. The result of characterization showed the sample with 8% RGO presented the optimum properties, such as visible-absorption, low band gap energy (2.1 eV) and a great surface area of as high as 130 m^2/g. Thereafter, the photocatalyst (CCTO – RGO (8%)) was applied to aid photodegradation of MO as a model of aqueous organic pollutants under visible-light irradiation. To optimize the efficiency, the photodegradation was modeled using multivariate semi-empirical methods such as RSM and ANN. The models optimized the effective level of the photodegradation factors including pH, photocatalyst amount, pollutant concentration and time of irradiation as well as their order of importance, which is crucial to industrial application scale-up. The result of optimized photodegradation indicated that 0.96 g/L of the photocatalyst removed 45 mg/L of the methyl-orange at pH 5.8 during 288 min of irradiation with 89% efficiency. This satisfactory performance along with the optimized method of photodegradation represents the potential of this photocatalyst as a powerful candidate toward scaling up for industrial applications. Moreover, the photodegradation has been scaled up for industrial applications by determination of the importance of the input effective variables according to the following order: organics > photocatalyst > pH > irradiation time.

REFERENCES

Abdollahi, Y., Abdullah, A. H., Zainal, Z. & Yusof, N. A. 2011a Photodegradation of m-cresol by zinc oxide under visible-light irradiation. *International Journal of Chemistry* **3** (3), p. 31.

Abdollahi, Y., Abdullah, A. H., Zainal, Z. & Yusof, N. A. 2011b Synthesis and characterization of manganese doped ZnO nanoparticles. *International Journal of Basic & Applied Sciences* **11** (4), 62–69.

Abdollahi, Y., Abdullah, A. H., Zakaria, A., Zainal, Z., Masoumi, H. R. F. & Yusof, N. A. 2012a Photodegradation of *p*-cresol in aqueous Mn (1%)-Doped ZnO suspensions. *Journal of Advanced Oxidation Technologies* **15** (1), 146–152.

Abdollahi, Y., Zakaria, A., Matori, K. A., Shameli, K., Jahangirian, H., Rezayi, M. & Abdollahi, T. 2012b Interactions between photodegradation components. *Chem Cent J.* **6** (100), 1–5.

Abdollahi, Y., Zakaria, A., Aziz, R. *et al.*. 2013a Optimizing Bi_2O_3 and Tio_2 to achieve the maximum non-linear electrical property of ZnO low voltage varistor. *Chemistry Central Journal* **7** (1), 137–143.

Abdollahi, Y., Zakaria, A., Abbasiyannejad, M., Masoumi, H. R. F., Moghaddam, M. G., Matori, K. A., Jahangirian, H. & Keshavarzi, A. 2013b Artificial neural network modeling of *p*-cresol photodegradation. *Chemistry Central Journal* **7** (96), 1–7.

Abdollahi, Y., Sairi, N. A., Aroua, M. K., Masoumi, H. R. F., Jahangirian, H. & Alias, Y. 2014a Fabrication modeling of industrial CO_2 ionic liquids absorber by artificial neural networks. *Journal of Industrial and Engineering Chemistry* **25**, 168–175.

Abdollahi, Y., Zakaria, A. & Nor Asrina, S. 2014b Degradation of high level m-cresol by zinc oxide as photocatalyst. *CLEAN–Soil, Air, Water* **42** (9), 1292–1297.

Acik, M., Lee, G., Mattevi, C., Chhowalla, M., Cho, K. & Chabal, Y. 2010 Unusual infrared-absorption mechanism in thermally reduced graphene oxide. *Nature Materials* **9** (10), 840–845.

Aviam, O., Bar-Nes, G., Zeiri, Y. & Sivam, A. 2004 Accelerated biodegradation of cement by sulfur-oxidizing bacteria as a bioassay for evaluating immobilization of low-level radioactive waste. *Applied and Environmental Microbiology* **70** (10), 6031.

Chen, K.-p. & Zhang, X.-w. 2010 Synthesis of calcium copper titanate ceramics via the molten salts method. *Ceramics International* **36** (5), 1523–1527.

Clark, J. H., Dyer, M. S., Palgrave, R. G., Ireland, C. P., Darwent, J. R., Claridge, J. B. & Rosseinsky, M. J. 2010 Visible light photo-oxidation of model pollutants using $CaCu_3Ti_4O_{12}$: an

experimental and theoretical study of optical properties, electronic structure, and selectivity. *Journal of the American Chemical Society* **133** (4), 1016–1032.

Devi, L. G. & Kavitha, R. 2013 A review on non metal ion doped titania for the photocatalytic degradation of organic pollutants under UV/solar light: role of photogenerated charge carrier dynamics in enhancing the activity. *Applied Catalysis B: Environmental* **140**, 559–587.

Dorraj, M., Zakaria, A., Abdollahi, Y., Hashim, M. & Moosavi, S. 2014 Optimization of Bi_2O_3, TiO_2, and Sb_2O_3 doped ZnO-based low-voltage varistor ceramic to maximize nonlinear electrical properties. *The Scientific World Journal* **2014**, 741034.

Dorraj, M., Abdollahi, Y., Said, S. B. M., Sabri, M. F. B. M., Sairi, N. A., Meng, W. P. & Abouzari-Lotf, E. 2015 Enhance protection of electronic appliances through multivariate modelling and optimization of ceramic core materials in varistor devices. *RSC Advances* **5** (27), 21384–21395.

Fröhlich, C. 2002 Total solar irradiance variations since 1978. *Advances in Space Research* **29** (10), 1409–1416.

Ghaffari, A., Abdollahi, H., Khoshayand, M., Bozchalooi, I. S., Dadgar, A. & Rafiee-Tehrani, M. 2006 Performance comparison of neural network training algorithms in modeling of bimodal drug delivery. *International Journal of Pharmaceutics* **327** (1), 126–138.

Kansal, S., Singh, M. & Sud, D. 2008 Studies on TiO_2/ZnO photocatalysed degradation of lignin. *Journal of Hazardous Materials* **153** (1), 412–417.

Martino, C. & Savage, P. 1997 Thermal decomposition of substituted phenols in supercritical water. *Ind. Eng. Chem. Res.* **36** (5), 1385–1390.

Martino, C., Savage, P. & Kasiborski, J. 1995 Kinetics and products from o-cresol oxidation in supercritical water. *Industrial & Engineering Chemistry Research* **34** (6), 1941–1951.

Propach, V. 1977 *Kristallstruktur von Ca0, 5Cu1, 5Ti2O6, Cu1, 5 TaTiO6 und CuTa2O6. Das spektroskopische Verhalten von Cu^{2+}-Ionen in kuboktaedrischer Umgebung*. *Zeitschrift für anorganische und allgemeine Chemie* **435** (1), 161–171.

Rakhshani, A. & Barakat, F. 1987 Optical constants of reactively sputtered cupric oxide films. *Materials Letters* **6** (1), 37–40.

Subramanian, M. & Sleight, A. 2002 $ACu_3Ti_4O_{12}$ and $ACu_3Ru_4O_{12}$ perovskites: high dielectric constants and valence degeneracy. *Solid State Sciences* **4** (3), 347–351.

Sun, H., Lin, S., Peng, T. & Liu, B. 2014 Microstructure and spectral characteristics of graphene oxide during reduction. *Integrated Ferroelectrics* **151** (1), 21–30.

Takeda, N. & Teranishi, K. 1988 Generation of superoxide anion radical from atmospheric organic matter. *Bulletin of Environmental Contamination and Toxicology* **40** (5), 678–682.

Thuillier, G., Hersé, M., Foujols, T., Peetermans, W., Gillotay, D., Simon, P. & Mandel, H. 2003 The solar spectral irradiance from 200 to 2400 nm as measured by the SOLSPEC spectrometer from the ATLAS and EURECA missions. *Solar Physics* **214** (1), 1–22.

Titelman, G., Gelman, V., Bron, S., Khalfin, R., Cohen, Y. & Bianco-Peled, H. 2005 Characteristics and microstructure of aqueous colloidal dispersions of graphite oxide. *Carbon* **43** (3), 641–649.

Wu, L., Yu, J. C. & Fu, X. 2006 Characterization and photocatalytic mechanism of nanosized CdS coupled TiO_2 nanocrystals under visible light irradiation. *Journal of Molecular Catalysis A: Chemical* **244** (1), 25–32.

Ye, F. & Ohmori, A. 2002 The photocatalytic activity and photo-absorption of plasma sprayed TiO_2-Fe_3O_4 binary oxide coatings. *Surface and Coatings Technology* **160** (1), 62–67.

First received 25 September 2017; accepted in revised form 4 January 2018. Available online 17 January 2018